

MAVIS: the impact of the mid-spatial frequency figure errors of optics on the astrometric error

Oleksandra Rebrysh^{a,b,*} Davide Greggio^{a,c} Jesse Cranney^{b,d,e}
Valentina Viotto^{a,c} Israel Vaughn^{d,e} Dionne Haynes^{d,e}
David Brodrick^{d,e} and François Rigaut^{d,e}

^aINAF - Osservatorio Astronomico di Padova, Padova, Italy

^bThe University of Padua, Department of Physics and Astronomy "Galileo Galilei", Padova, Italy

^cADONI - ADaptive Optics National Laboratory, Italy

^dAustralian National University, Research School of Astronomy and Astrophysics,
Advanced Instrumentation Technology Centre, Canberra, Australia

^eAstralis Instrumentation Consortium, Australia

ABSTRACT. Mid-spatial frequency figure errors (MSFEs) occurring on optical surfaces are an unavoidable issue that may influence the performance of an optical system. In this paper, we present the results of an analysis dedicated to the impact of MSFE of the optical surfaces on the relative astrometric error. The method involves an almost end-to-end simulation, encompassing the calibration of the optical distortions. Although the analysis described here is primarily focused on the specific case of the MCAO-Assisted Visible Imager and Spectrograph (MAVIS) instrument, it is worth noting that the same methodology can be applied to other instruments as well. To provide context, MAVIS, short for multi-conjugate adaptive optics-assisted visible imager and spectrograph, represents the next-generation instrument designed for the Very Large Telescope. The distortions considered in the analysis stem from the optical components of the adaptive optics module of MAVIS. The results take into account both field rotation and wavelength dependencies. Relative astrometric errors are computed across different separations between sources. Furthermore, we analyze distortions introduced by the atmospheric dispersion corrector, factoring in the zenith angle dependence. A similar in-depth analysis is conducted for the imager components. This approach offers a comprehensive understanding of the intricate interplay between MSFE of optical components and astrometric precision.

© The Authors. Published by SPIE under a Creative Commons Attribution 4.0 International License. Distribution or reproduction of this work in whole or in part requires full attribution of the original publication, including its DOI. [DOI: [10.1117/1.JATIS.11.1.018002](https://doi.org/10.1117/1.JATIS.11.1.018002)]

Keywords: MAVIS; astrometry; mid-spatial frequency; distortion

Paper 24111G received Jul. 17, 2024; revised Dec. 24, 2024; accepted Jan. 7, 2025; published Jan. 29, 2025.

1 Introduction

Recent developments in multi-conjugate adaptive optics (MCAO) techniques allow us to make a significant breakthrough in the building of the next-generation instrumentation for ground-based telescopes.¹ Instruments that will benefit from the MCAO are, for instance, Multi-AO Imaging Camera for Deep Observation (MICADO),² served by MCAO For Extremely Large Telescope (ELT) Observations (MORFEO)³ on the ELT, Narrow Field InfraRed Adaptive Optics System (NFIRAOS)⁴ on the Thirty Meter Telescope (TMT) and MCAO-Assisted Visible Imager and Spectrograph (MAVIS)⁵ on the Very Large Telescope (VLT). MAVIS and MICADO complement each other by addressing similar science cases, enabling a comprehensive multi-wavelength approach—spanning from visible to infrared—for studying astronomical phenomena.

*Address all correspondence to Oleksandra Rebrysh, oleksandra.rebrysh@inaf.it

A pivotal objective for both of these instruments is achieving high-precision astrometry.^{6,7} Although the launch of the Global Astrometric Interferometer for Astrophysics (GAIA) space telescope has yielded impressive results,⁸ the astrometric study still faces some limitations. One of these limits is crowded stellar fields within and beyond our galaxy. However, the promising astrometric precision and the high angular resolution offered by new instrumentation designed for large telescopes hold the potential to overcome this limitation. Consequently, the primary scientific focus of MAVIS is linked to addressing challenges posed by crowded stellar environments, particularly within globular clusters (GCs). More specifically, the main goal is to search for intermediate-mass black holes in the GC cores.⁹ To achieve this objective, accurate astrometry is required. MAVIS has a relative astrometric requirement of 150 μas defined for two isolated point sources separated by 1 arcsec. This final astrometric error includes contributions from various system-related factors, such as the telescope and Natural Guide Stars (NGS) probe movements, as well as from the data extraction process.¹⁰ Among these contributors—and the primary focus of this paper—are distortions caused by the mid-spatial frequency figure errors (MSFEs) of optical elements.¹¹ This work is part of a broader research focused on the astrometric error budget requirements for MAVIS. Other sources that can affect the astrometric accuracy of the instrument, including AO-related errors, plate scale variations, temperature variations, or astrometric retrieval, are under separate studies.¹²

MSFEs are unavoidable artifacts on an optical surface that occur during sub-aperture grinding or polishing stages.¹³ These errors can significantly degrade image quality and introduce distortions that directly impact the precision of astrometric measurements. Consequently, controlling MSFEs becomes imperative.

Generally, surface errors introduced by any manufacturing process can be classified into three categories:¹⁴ (1) low-spatial frequency (traditional figure error), (2) mid-spatial frequency (ripple), and (3) high-spatial frequency (microroughness). Decomposing the surface errors into these three regimes simplifies the analysis of their impact on the overall instrument performance. For instance, low-frequency errors can be represented using standard Zernike polynomials, whereas microroughness is explored through the application of scattering theory.¹⁵

Our research is primarily centered on the examination of the MSFEs in the optics of MAVIS and its potential implications for the astrometric precision of the instrument. In Sec. 2, we provide a detailed overview of the methodology employed for simulating the MSFE and generating distortion maps. Section 3 delves into the current findings of our study, shedding light on the intricate relationship between the MSFE and astrometric accuracy of MAVIS. Although the real calibration will be conducted for the entire instrument, we divided the analysis into three parts. This approach allows us to independently estimate the contributions of the Adaptive Optics Module (AOM), the Atmospheric Dispersion Corrector (ADC) only, and the imager. Several factors influence this decision: the AOM and the imager are distinct subsystems, and there is a preference to keep them separate for subsequent testing during the Assembly, Integration and Verification (AIV) phase, and the distortions of the ADC may exhibit dependence on the zenith angle (ZA). Conducting separate analyses facilitates the interpretation of the results. Finally, we conclude with a comprehensive discussion and conclusions of our research in Sec. 4, drawing important insights and implications for future work in this field.

2 Method and Simulation Approach

Given that MSFEs are not comprehensively addressed through low-frequency analysis or scattering studies, bridging the gap between these two regimes involves modeling MSFE as perturbations to the optical surface.¹⁴ These perturbations can be generated by applying the inverse Fourier transform of a 2D power spectral density (PSD) function with a random phase.¹⁶ Typically, the PSD of polished optical surfaces can be well approximated by a power law of the form:

$$\text{PSD} \propto \sqrt{\frac{1}{(u^2 + v^2)^\beta}},$$

where u and v are the spatial frequencies in the horizontal and vertical directions, and β is the slope coefficient of the PSD. The actual value of the slope generally depends on the

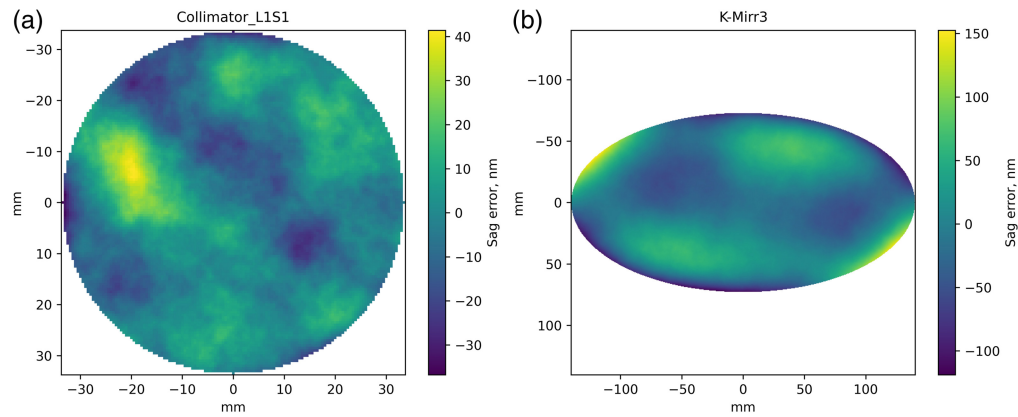


Fig. 1 Surface figure error maps of the first lens of the collimator (a) and the third K-mirror (b). The amplitude of the MSFE component is equal to 9-nm RMS, whereas the amplitude of the low-order Zernike component changes for every optical surface and depends on the tolerance allocated for the overall surface figure error.

manufacturing process. However, typical values for precision polished optics are in the range $1.5 \leq \beta \leq 2.5$.¹⁷ In the case of our simulation, the β value was chosen to be equal to 2.4.

Considering it, we generate figure error maps for the optical elements in the AOM of MAVIS, which we subsequently insert into the optical model to calculate the distortion via ray-tracing simulations. To model the figure error of each optical surface, we combine a low-spatial frequency map generated as a random combination of Zernike polynomials and a medium-frequency map generated using the PSD method. Examples of such maps are presented in Fig. 1. Optical components, for which the maps are shown, are part of the common path of the AOM and are located as depicted in the layout in Fig. 2.¹⁸ The figure also displays some components of the NGS and laser guide stars (LGS) channels, along with the Calibration Unit (CU). Nevertheless, these elements are not considered in the present study.

The sizes of the optical elements and the corresponding footprints are shown in Table 1.

There are two types of apertures for the AOM optical elements, and they are treated slightly differently. We utilize the first 36 Zernike polynomials, as per Noll numbering, for circular apertures, whereas for elliptical apertures, we apply only 15 polynomials defined by Mahajan and Dai.¹⁹ In total, there are three elements with elliptical apertures in the AOM, collectively forming the K-mirror used for the field de-rotation. The amplitude of the MSFE equals 9-nm root-mean-square (RMS) for both types of apertures. This amplitude is in good agreement with the high-end

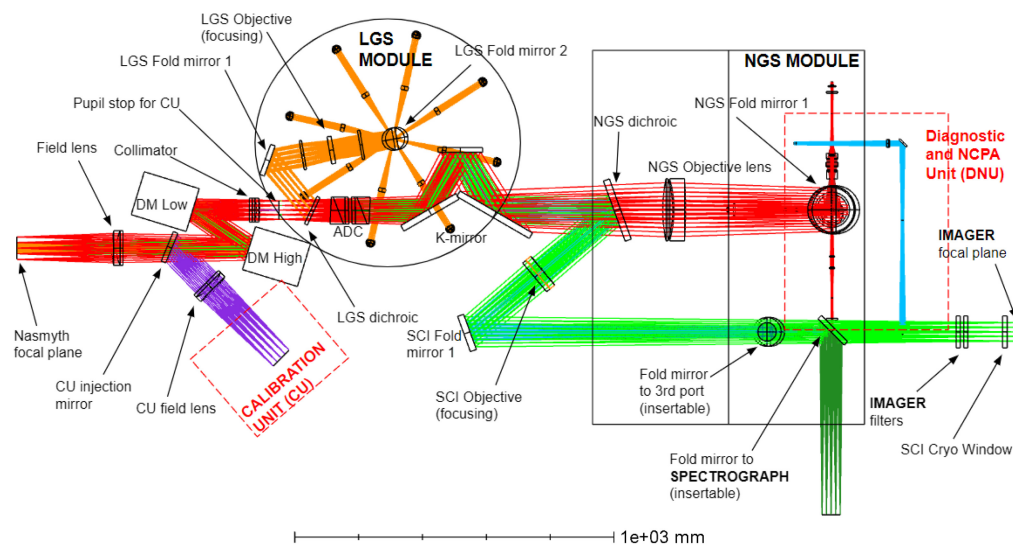


Fig. 2 Layout of the optical design of the AOM of MAVIS.

Table 1 Characteristics of the optical elements used in the simulations.

Optical element	Clear diameter (mm)	Footprint size (mm)
Field lens 1	96	20
Field lens 2	96	20
Collimator lens 1	67	55
Collimator lens 2	67	56
Collimator lens 3	67	57
LGS dichroic	84	57
ADC prism 1	85	57
ADC prism 2	85	57
K-mirror 1	100 × 50 (elliptical)	57
K-mirror 2	70 × 61 (elliptical)	57
K-mirror 3	131 × 68 (elliptical)	57
NGS dichroic	180	57
SCI objective lens 1	105	57
SCI objective lens 2	105	57
SCI fold mirror	105	52
Imager filter 1	100	5
Imager filter 2	100	4
SCI Cryo window	100	1

finishing specifications provided by manufacturers.²⁰ It is important to mention that, in the process of map generation, we intentionally omit the first four Zernike terms, which represent piston, tip, tilt, and defocus. Piston, tip, and tilt are excluded as they are not part of the surface figure error specifications, whereas defocus is omitted because it primarily affects the average instrument plate scale without introducing higher-order spatial distortions.

After successfully generating the figure error maps, we integrate them into the optical model of the instrument using the software Ansys Zemax OpticStudio.²¹ This software is employed to perform ray tracing throughout the entire system to calculate the distortion maps. We run the ray tracing over the entire scientific field of view (FoV), which has a radius of 15", utilizing a pupil sampling of 150 × 150 rays and using 40 × 40 field points to accurately capture the mid-spatial frequency perturbations. The distortion generated by MSF figure errors depends on wavelength and field rotation. The wavelength dependence arises from the presence of refractive components. On the other hand, the dependence on field rotation is linked to sky rotation in an alt-azimuth-mounted telescope. This rotation causes the beam footprint on all optical elements upstream of the de-rotator to rotate with the parallactic angle, thereby illuminating different portions of the optical surfaces. These effects need to be properly calibrated as soon as the variation of the distortion map induced by them exceeds the tolerances. To simulate this aspect, in our analysis, we account for the field rotation, considering the range of angles from 0 to 30 deg, and we account for chromaticity by producing distortion maps covering the full wavelength range from 370 to 1000 nm.

As the last step, we use the obtained distortion maps as an input for MAVISIM. MAVISIM is the image simulation tool for MAVIS, and it allows us to simulate the distortion calibration procedure necessary for our analysis. This procedure is based on a differential method aimed at mitigating the impact of manufacturing errors on distortion retrieval.²² In the real calibration case, we will have an Astrometric Calibration Module (ACM) placed in front of the Field lens,

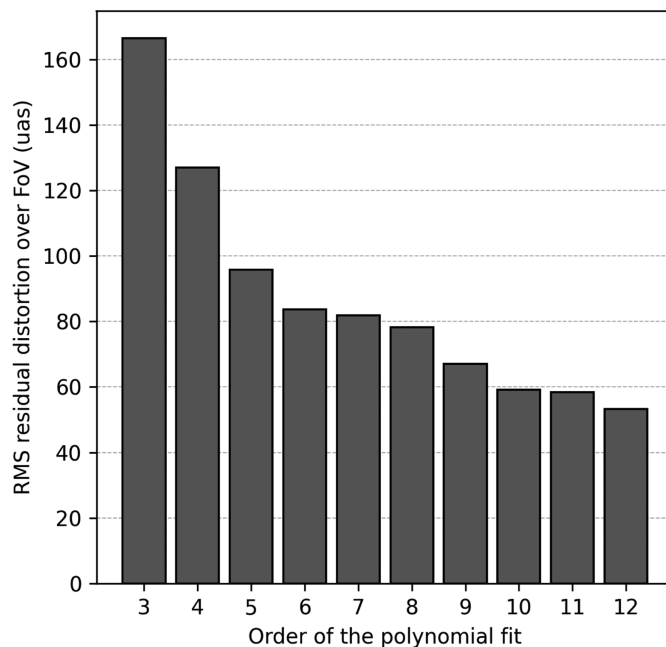


Fig. 3 RMS residual distortion after calibration for the reference case: 0 deg field rotation at $\lambda = 550$ nm.

coincident with the input Nasmyth focal plane. The ACM contains a pinhole mask with 1607 sources that can be shifted in x and y . These offsets allow us to obtain the Jacobian of the distortion field, which is then fitted using bivariate polynomials as a set of basis functions.²³ Despite being quite beneficial, this calibration method has a drawback. As it is based on first derivatives, it introduces internal errors due to linearization, along with other potential error sources, resulting in a noise floor in all the distortion maps obtained.

The calibration for all our distortion maps is done in the end-to-end mode using the distortion map at a field rotation angle of $\alpha_{\text{rot}} = 0$ deg and $\lambda = 550$ nm as the calibration reference. The residuals of the calibration procedure as a function of the order of the fitting polynomials are shown in Fig. 3. As it can be seen from the figure, the use of polynomial orders greater than 9 does not bring in much of an improvement, and the residuals are dominated by other noise sources such as the centroiding noise on the image of the pinhole mask. Despite this, we accepted the 11th-order polynomial fit in the subsequent simulations. Using higher-order polynomials is not advisable as they may amplify noise in the calibration procedure. The residuals after the calibration for the considered cases are presented in Sec. 3.

To achieve the stated aim of this work—the evaluation of the relative astrometric error—we randomly generate 400 point sources over the full FoV. The astrometric error is then calculated as a function of the distance between sources, comparing their true separation values with the ones reconstructed after the calibration procedure.

3 Results

3.1 Post-focal Relay Optics

The first part of the analysis considers all the optics in the post-focal relay (PFR) of MAVIS. Namely, surface figure error maps were added to the following elements: field lens, collimator, LGS dichroic, ADC, K-mirror, NGS dichroic, science objective, and science fold mirror (see Fig. 2).¹⁸ Following the procedure described in Sec. 2, we extracted the residual distortion after the calibration. An example of the obtained residual distortions for the static scenario is presented in Fig. 4(a). The values of the RMS residuals in this case are slightly higher than $50 \mu\text{as}$.

The RMS residual distortion over the full scientific FoV is presented in Fig. 4(b). Although no significant wavelength dependence is observed, the distortions appear to be more sensitive to it at smaller field rotation angles. Taking into account the fact that we carry out the calibration at

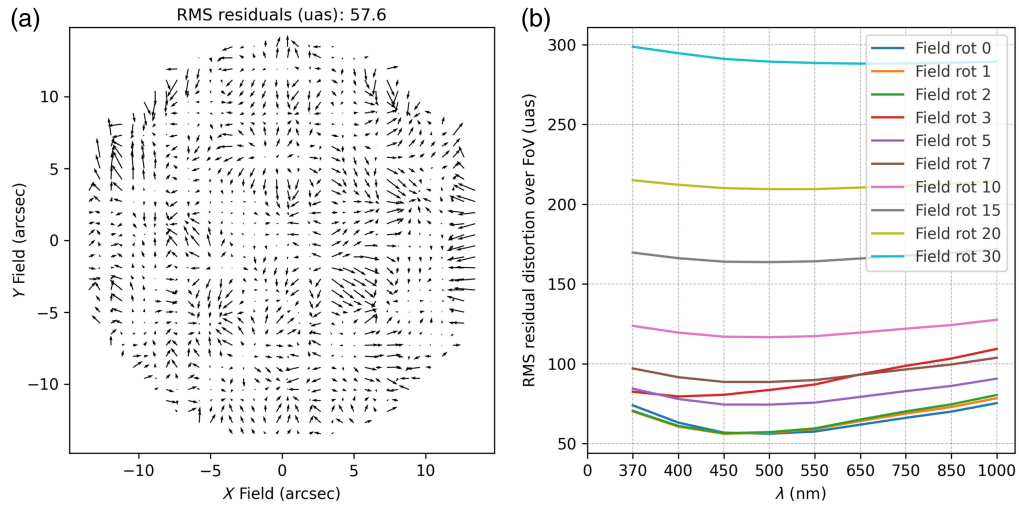


Fig. 4 (a) Residual distortion maps after calibration with 11th-order polynomial. Here: the field rotation angle α_{rot} is 0 deg, $\lambda = 550$ nm. (b) RMS residual distortion over the full scientific FoV after calibration with an 11th-order polynomial.

$\lambda = 550$ nm, it is expected to get the lowest RMS residual at that wavelength. Despite some variations in values, the lowest residuals are indeed around the calibration wavelength. Therefore, the expected residual distortion due to figure errors of the optical elements of the AOM common path is in the range from 50 to 300 μas RMS depending on field rotation angle and wavelength. As mentioned in the introduction, the astrometric budget includes contributions from various parameters, with PSF variability and tip-tilt residuals being among the most significant sources of error.⁷ Therefore, the obtained results highlight the necessity of frequent calibrations to minimize the contribution of MSF distortions. Although producing a complete budget for the astrometric error is beyond the scope of this paper, recalibrating distortions every 7 to 10 deg could reduce the astrometric error due to MSF distortions by at least 20%.

The main aim of this work is to estimate the relative astrometric error due to distortions induced by optics. Figure 5 shows the foreseen astrometric error as a function of the separation between pairs of stars. We considered a range of the stars' separations to examine the behavior of the final astrometric error after the calibration. It is clearly seen from the plots that bigger rotation angles lead to bigger astrometric errors. Moreover, there is a trend in all of the cases, showing

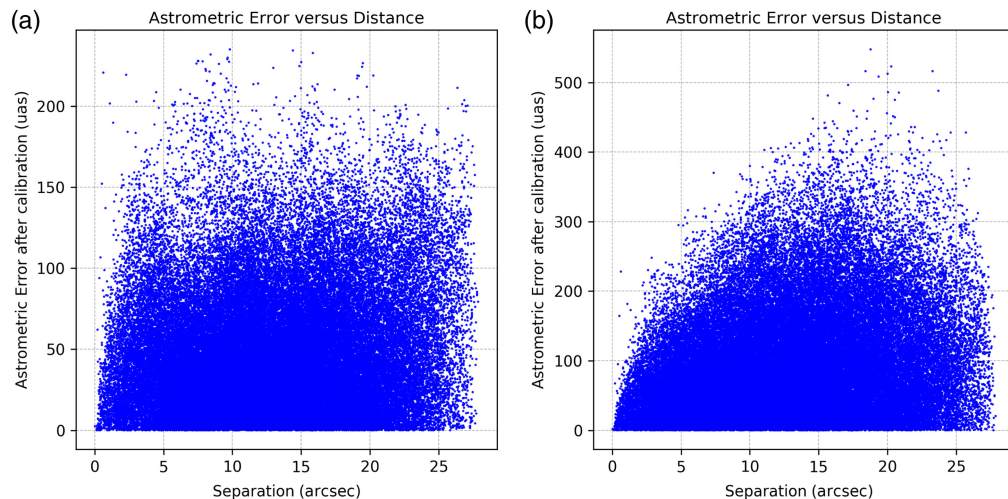


Fig. 5 Astrometric error as a function of star separation after calibration with the 11th-order polynomial fit to the static distortion map at 550 nm. (a) $\alpha_{\text{rot}} = 0$ deg, $\lambda = 550$ nm; (b) $\alpha_{\text{rot}} = 10$ deg, $\lambda = 550$ nm.

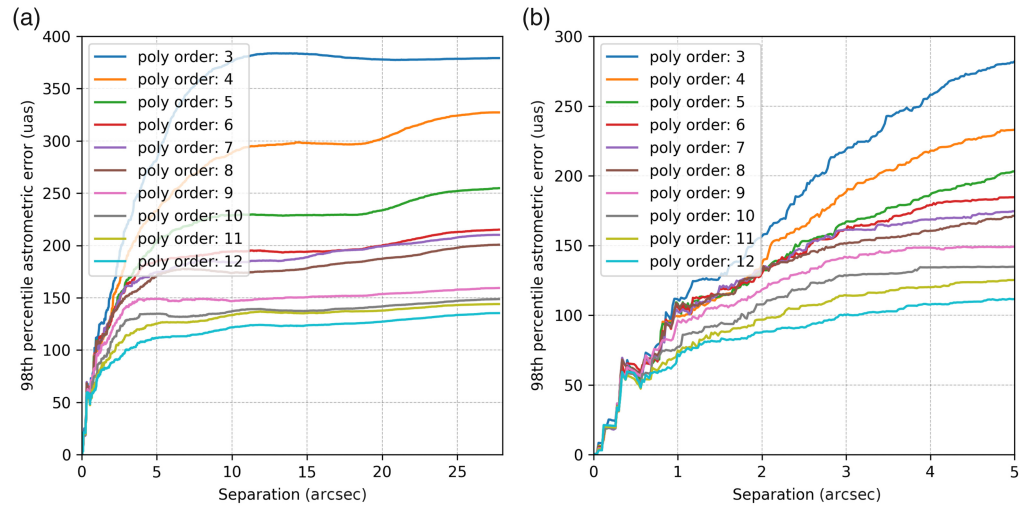


Fig. 6 (a) 98th percentile astrometric error as a function of separation between sources for $\alpha_{\text{rot}} = 0$ deg and $\lambda = 550$ nm. (b) Zoomed-in plot for the separation between 0 and 5 arcsec.

bigger uncertainties in the astrometric measurements for larger separation between sources. Such behavior is due to the fact that, for larger separations, the points are likely farther from the center, leading to greater relative displacements caused by field rotation. In addition, the decrease in values after a certain separation is due to the smaller number of points at the largest distances.

A better understanding of the derived results can be provided by Figs. 6 and 7, which show the 98th percentile of the astrometric error for different wavelengths and field rotation angles. The calculation is done for all pairs of stars with a distance smaller than a certain threshold distance d . Figure 6 demonstrates that the 11th- and 12th-order polynomial fits yield the best results for the relative astrometric error. However, as we chose to use the 11th-order polynomial for our fit, Fig. 7 presents the astrometric error for 1 and 15 arcsec separation between sources in dependence of the field rotation angle and the wavelength for this case. It is explicit that the dependence on field rotation is stronger, leading to higher astrometric error for bigger angles. However, sources separated by 1 arcsec exhibit fluctuations in values due to the lower sensitivity of the distortion to the field rotation angles at such small distances. Talking about wavelength dependence, it is almost untraceable with an exception for the blue end of the wavelength range. The errors in UB bands are bigger compared with other wavelengths for the same field rotation angle. Nevertheless, looking at the results, we see that the astrometric error is in the range 65 to 105 μas for 1 arcsec separation and 80 to 720 μas for 15 arcsec.

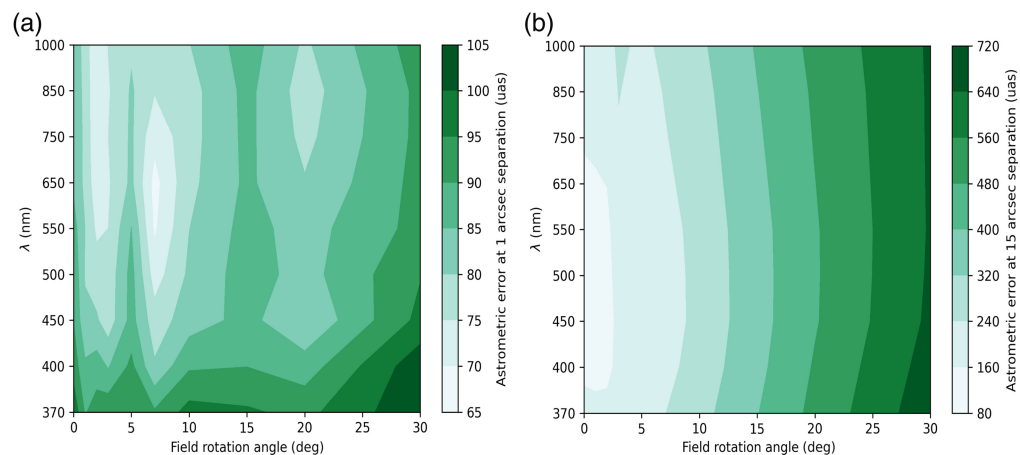


Fig. 7 98th percentile relative astrometric error at 1 arcsec (a) and 15 arcsec (b) separation as a function of wavelength and field rotation angle.

3.2 Atmospheric Dispersion Corrector Only

As the refractive index of the atmosphere, n_{atm} , depends on the wavelength, it could lead to significant challenges in achieving precise astrometry. Atmospheric dispersion changes the apparent angular distance between observed sources based on their color differences. In addition, it elongates the shape of the PSF along the zenith,²⁴ reducing the Strehl ratio and causing issues in the PSF fitting. To overcome these issues, MAVIS uses the ADC composed of two counter-rotating Amici prisms.²⁵ However, the use of the ADC may also impact the astrometric error because, due to the rotation of the prisms, this optical element can introduce varying distortion across the FoV. Therefore, we performed a dedicated analysis using the method described in Sec. 2.

The simulation, based on ray tracing, accounts for the atmospheric dispersion and its correction by the ADC. We used the Ciddor model for the refractive index of air.²⁶ We calculated distortion maps for several zenith distances of observation and wavelengths, considering only monochromatic sources. To only capture the distortion variation produced by the ADC, the field rotation was not considered in this analysis.

Thus, summarizing the procedure for the ADC:

- Surface figure error perturbations were introduced only to the ADC optical surfaces.
- No field rotation was introduced.
- Calibration is done to different ZA.

We consider a range of ZA from 0 to 65 deg. Figure 8 and Table 2 present the results for the RMS distortion residuals. Calibration is performed for each ZA, with a comparison to neighboring angles. The order of the polynomial used for fitting is the same as that used for the PFR optics.

The obtained results show that, when observing at a specific ZA and calibrating to it, the residual distortion is minimal, ~ 35 to $36 \mu\text{as}$. However, as one deviates from the calibration angle, the expected residuals increase. The distortion residuals are particularly sensitive to small deviations from the calibration angle, especially as the observation approaches the horizon. Therefore, in such cases, the difference between the observation and calibration angles should be significantly smaller than the step considered in this analysis.

The last part regarding the distortion of the ADC is to check if there is some wavelength dependence present. It was evaluated using 550 nm as the calibration wavelength to be consistent with the rest of the study. The resulting plot for the cases of ZA = 15, 30, and 45 deg calibrated to the ZA of 30 deg is shown in Fig. 9. This plot contains information about both chromatic and achromatic components. The general behavior is similar to the case of PFR optics (e.g., Fig. 7) with the blue end being the most sensitive to calibration, especially when observing far from the

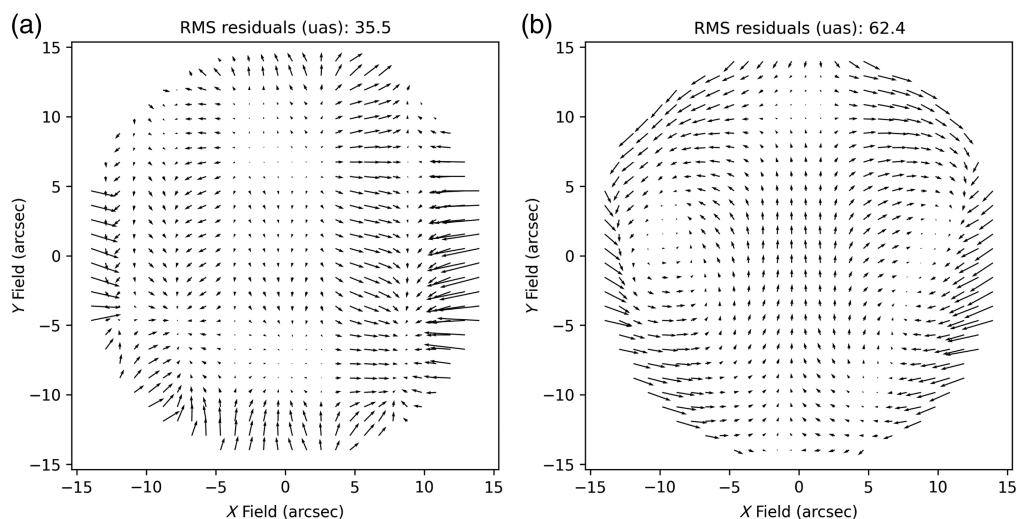
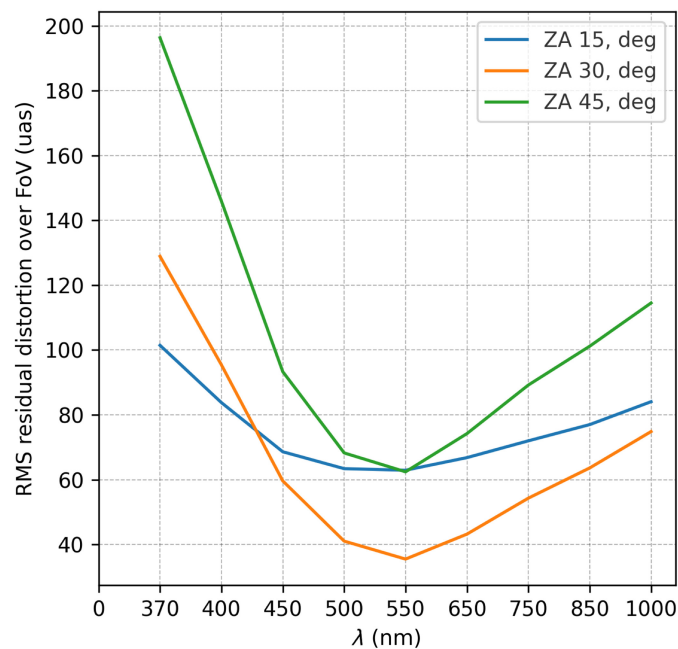


Fig. 8 Examples of the residual distortion maps at 550 nm for the ZA of 30 deg (a) and 45 deg (b) with the calibration to the distortion map at ZA = 30 deg.

Table 2 RMS residual distortion after calibration for different ZAs. Units are μas . Diagonal values are the ones calibrated to the proper ZA.

		ZA (deg)					
		0	15	30	45	51	65
Calibration ZA (deg)	0	35.8	53.5	—	—	—	—
	15	60.2	35.2	56.7	—	—	—
	30	—	62.9	35.5	62.4	—	—
	45	—	—	65.6	35.7	44.5	—
	51	—	—	—	44.3	35.6	192.7
	65	—	—	—	—	183.0	35.8

**Fig. 9** RMS residual distortion after calibration for ADC only as a function of wavelength. Data for the cases of 15, 30, and 45 deg ZA calibrated to the ZA = 30 deg and $\lambda = 550$ nm.

zenith. However, the calibration method itself isolates the achromatic component by considering separate distortion maps for each wavelength. Therefore, the residual at 550 nm represents only the distortion component. Interestingly, the residuals are smaller in the wavelength range from 370 to 430 nm for ZA = 15 deg compared with ZA = 30 deg, which was used for calibration. This is likely due to the chromatic error counterbalancing the variation of distortion produced at the different ZA.

In this section, we presented the impact of the MSFE of the ADC optical surfaces on the astrometric error due to the rotation of the ADC prisms during observations. This rotation introduces variability in the distortion map on the imager. In addition, the ADC contributes to image wobble and low-order distortions, such as anamorphic plate scale variations.²⁷ In MAVIS, these image motions can be detected by the NGS wavefront sensor and are partially corrected by the AO loop. However, the chromatic dependence of these motions, which is propagated through the deformable mirrors (DMs) by the low-order AO loop, cannot be fully compensated. This limitation may result in small variations in plate scale and pointing on the imager focal plane. Plate scale variations can be corrected if at least three astrometric reference stars are available in the

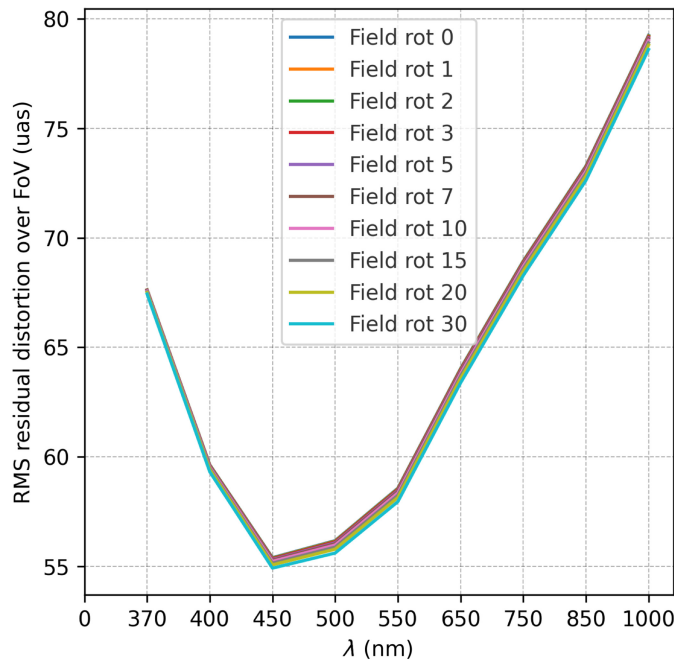


Fig. 10 RMS distortion residual as a function of wavelength. Calibration was done to the static distortion map at 550 nm, using the 12th-order polynomial fit.

frame. Nevertheless, variations occurring during the exposure time can lead to PSF smearing, which partially reduces the astrometric accuracy of the instrument. Given the complexity of ADC-induced distortions and their interaction with the AO loop, a more detailed investigation has been undertaken as a separate study, which lies beyond the objectives of this paper.

3.3 Imager Filters and the Cryo Window

In the framework of MAVIS, the imager essentially employs a detector at the F/35 image plane provided by the AOM, without the use of reimaging optics. However, two filters and the cryostat window are planned to be incorporated.²⁸ Therefore, it is important to assess the impact of distortions arising from the MSFE of their optical surfaces on the overall astrometric error. All elements of the imager are positioned after the K-Mirror; thus, the field rotation dependence should be minimal or absent altogether. Indeed, the results confirm this expectation.

We conducted the analysis by calibrating the distortion maps to a wavelength of 550 nm, consistent with previous cases. However, due to the imager elements being located very close to the focal plane, the relationship between distortion residuals and wavelength becomes more complex. For the same reason, the amplitude of distortions stemming from the MSFE of the filters and the cryo window is also greater. To address this, we found it beneficial to use a higher-order polynomial for calibration. We opted for a 12th-order polynomial fit, which captures the complex distortions slightly better than the 11th-order fit. The results for the RMS residual distortions are presented in Fig. 10, which shows the wavelength dependence. The minimum of the RMS residuals is slightly shifted relative to the calibration wavelength. Although the difference in values is small, this shift could be explained by numerical uncertainties in the method.

The results for the relative astrometric error as a function of field rotation and wavelength are presented in Fig. 11. It can be observed that the values remain almost constant across all considered rotation angles, thus confirming the stabilization of the field by the K-Mirror. The range of the expected astrometric error is from 76 to 89 μas for sources 1 arcsec away from each other and from 120 to 200 μas for sources separated by 15 arcsec.

4 Discussion and Conclusion

We have conducted an analysis of the distortions caused by the MSFE of the optics of the AOM of MAVIS. Being an unavoidable artifact, these errors may have a significant impact on the

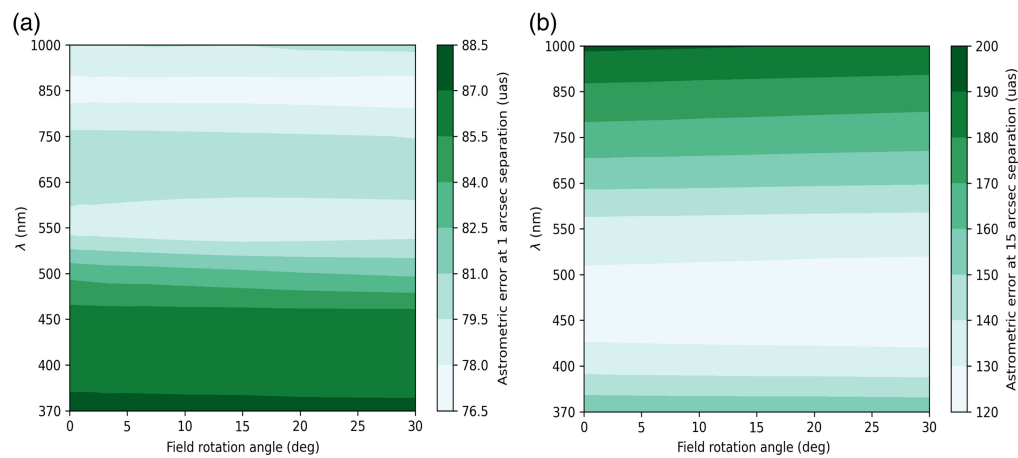


Fig. 11 98th percentile astrometric error at 1 arcsec (a) and 15 arcsec (b) separation as a function of wavelength and field rotation. Calibration was done to the static distortion map at 550 nm.

astrometric performance and hence should be accurately controlled and calibrated. The performed analysis was divided into three parts covering different optical elements of the AOM and the imager. It was found that the integrated distortions, discussed in Sec. 3.1, are strongly dependent on the field rotation angle, whereas the wavelength dependence is barely perceptible except for the UB-bands. The results can be used, based on the required astrometric accuracy, to place a limit to the maximum acceptable field rotation angle before re-calibration is needed. Our findings suggest that calibration should occur approximately every 10 deg of field rotation.

Taking into account the ZA dependence on the performance of the ADC, we carried out a separate analysis. It was shown that the distortion is bigger for observations closer to the horizon. Hence, more frequent calibrations may be required in this case.

Including the imager elements in the analysis turns out to be a challenging task. Being close to the focal plane, the distortions stemming from the imperfections of the imager's elements are more pronounced and more strongly affect the astrometric error. We increased the polynomial order fitting to get reasonable calibration results. Therefore, based on our results, the order of polynomials used in the real calibration case should be at least 12. However, although higher-order polynomials are beneficial for capturing the high-frequency distortions produced by the imager optics, the propagation of noise must also be considered.

The challenges posed by the astrometric requirements for future instrumentation necessitate precise calibration of instrument distortions. To accurately assess astrometric performance and the extent to which various distortion sources can be calibrated, employing an end-to-end simulation approach for deriving and validating instrument requirements is essential. This task is exceedingly challenging, and to the best of our knowledge, such comprehensive analysis has not been widely adopted so far. In this paper, we focused on the static and dynamic components of distortions produced by the MSFE of optical surfaces. Even though the results are not exhaustive, they provide valuable insights for setting requirements on the MSFE of optical surfaces. They also help in determining the most appropriate degree of polynomial for accurate distortion map reconstruction, assessing when re-calibration is necessary, and thereby optimizing the use of observation time.

The methodology described in this paper can be applied to any optical instrument to estimate and calibrate distortions present in the system. While addressing the specific astrometric requirements of MAVIS, this study also provides a flexible framework for assessing and mitigating MSFE in other high-precision optical systems. The approach, which integrates figure error maps into optical models and employs detailed ray tracing to analyze distortion effects, offers a robust method for ensuring accurate calibration and performance validation. These techniques are particularly useful for instruments requiring precise astrometric calibration as they provide a systematic way to quantify and correct existing optical distortions, ensuring accurate scientific measurements.

Disclosures

The authors declare there are no financial interests, commercial affiliations, or other potential conflicts of interest that have influenced the objectivity of this research or the writing of this paper.

Code and Data Availability

The code used to ray trace through the optical system and obtain distortion maps is available on GitHub https://github.com/alphaCassi/OpticalDesignAnalyses/tree/main/MSF_simulation. The code used for calibration is also available on GitHub <https://github.com/smonty93/MAVISIM>.

Acknowledgments

The MAVIS Astralis consortium nodes received funding under the Australian Government's National Collaborative Research Infrastructure Strategy (NCRIS) Program via Astronomy Australia Ltd (AAL). The MAVIS Italian nodes are supported by recurrent funds from INAF. The MAVIS hardware is funded by ESO, the Australian Research Council (through the LIEF Grant No. LE220100037), NCRIS and the Australian National University, as well as a number of Australian Universities. This work benefited from support by the French government under the France 2030 investment plan, as part of the Initiative d'Excellence d'Aix-Marseille Université AMIDEX (Grant No. AMX-22-RE-AB-151) and the Action Spécifique Haute Résolution Angulaire (ASHRA) of CNRS/INSU.

References

1. F. Rigaut and B. Neichel, "Multiconjugate adaptive optics for astronomy," arXiv:2003.03097 (2020).
2. R. Davies et al., "MICADO: the multi-adaptive optics camera for deep observations," *Messenger* **182**, 17–21 (2021).
3. L. Busoni et al., "MORFEO enters final design phase," in *Adaptive Optics for Extremely Large Telescopes (AO4ELT7)*, p. 129 (2023).
4. J. Crane et al., "NFIRAOS adaptive optics for the Thirty Meter Telescope," *Proc. SPIE* **10703**, 107033V (2018).
5. F. Rigaut et al., "MAVIS on the VLT: a powerful, synergistic ELT complement in the visible," *Messenger* **185**, 7–11 (2021).
6. G. Rodeghiero et al., "Performance and limitations of using ELT and MCAO for 50μ as astrometry," *J. Astron. Telesc. Instrum. Syst.* **7**, 035005 (2021).
7. S. Monty et al., "The MAVIS Image Simulator: predicting the astrometric performance of MAVIS," *Proc. SPIE* **11447**, 1144756 (2020).
8. A. G. A. Brown et al., "Gaia early data release 3. Summary of the contents and survey properties," *AAP* **649**, A1 (2021).
9. S. Monty et al., "Towards realistic modelling of the astrometric capabilities of MCAO systems: detecting an intermediate-mass black hole with MAVIS," *Mon. Not. R. Astron. Soc.* **507**, 2192–2207 (2021).
10. S. Trippe et al., "High-precision astrometry with MICADO at the European Extremely Large Telescope," *Mon. Not. R. Astron. Soc.* **402**, 1126–1140 (2010).
11. I. J. Vaughn et al., "Statistical basis functions for modelling mid-spatial frequency errors in asphere manufacturing," *Proc. SPIE* **13100**, 1310015 (2024).
12. O. Rebrysh et al., "MAVIS: optical distortions of the NGS WFS channel and their impact on the plate scale variation during tracking," *Proc. SPIE* **13019**, 130190B (2024).
13. M. Pohl et al., "Mid-spatial frequency error generation mechanisms and prevention strategies for the grinding process," *J. Eur. Opt. Soc. - Rapid Publ.* **16**, 19 (2020).
14. R. N. Youngworth and B. D. Stone, "Simple estimates for the effects of mid-spatial-frequency surface errors on image quality," *Appl. Opt.* **39**, 2198–2209 (2000).
15. J. E. Harvey and C. L. Vernold, "Transfer function characterization of scattering surfaces revisited," *Proc. SPIE* **3141**, 113–127 (1997).
16. J. E. Hayden and D. A. Content, "PSD data analysis and algorithm development," *Proc. SPIE* **10316**, 103160S (2007).
17. S. G. Alcock et al., "Using the power spectral density method to characterise the surface topography of optical surfaces," *Proc. SPIE* **7801**, 780108 (2010).
18. D. Greggio et al., "MAVIS Adaptive Optics Module: optical configuration and expected performance," *Proc. SPIE* **12185**, 121856P (2022).
19. V. N. Mahajan and G.-M. Dai, "Orthonormal polynomials in wavefront analysis: analytical solution," *J. Opt. Soc. Amer. A* **24**, 2994 (2007).

20. X. Nie et al., “Combined fabrication process for high-precision aspheric surface based on smoothing polishing and magnetorheological finishing,” *Proc. SPIE* **9281**, 928111 (2014).
21. D. C. O’Shea and J. L. Bentley, *Designing Optics using Zemax OpticStudio*, SPIE Press, Bellingham, Washington (2024).
22. J. Cranney et al., “MAVIS: astrometric calibration technique,” *Proc. SPIE* **12185**, 1218567 (2022).
23. J. Cranney et al., “MAVIS: astrometric and NCPA calibration plan,” in *Adaptive Optics for Extremely Large Telescopes (AO4ELT7)*, p. 64 (2023).
24. J. A. van den Born, W. Jellema, and E. Dijkstra, “Demonstration of an imaging technique for the measurement of PSF elongation caused by Atmospheric Dispersion,” *Mon. Not. R. Astron. Soc.* **512**, 5812–5822 (2022).
25. D. Greggio et al., “Optical design of a broadband atmospheric dispersion corrector for MAVIS,” *Proc. SPIE* **11447**, 1144755 (2020).
26. P. E. Ciddor, “Refractive index of air: new equations for the visible and near infrared,” *Appl. Opt.* **35**, 1566 (1996).
27. A. C. Phillips et al., “The Infrared Imaging Spectrograph (IRIS) for TMT: the ADC optical design,” *Proc. SPIE* **9908**, 9908A1 (2016).
28. E. Simon et al., “MAVIS: imager and spectrograph,” *Proc. SPIE* **12184**, 1218409 (2022).

Oleksandra Rebrysh is a PhD student at the University of Padova in association with INAF. Currently, she works on the MAVIS project contributing to the optical design finalisation and different verification and control analyses of the adaptive optics module of the instrument. In addition, she is one of the organizers of the annual NYRIA workshop for young scientists in astronomical instrumentation.

Davide Greggio is a senior astrophysicist specializing in the design and analysis of optical systems for Astronomy. He earned his PhD (2017) and MS (2013) degrees in astronomy from the University of Padova. He has contributed to the development of optical designs for several astronomical instruments for 8-m-class telescopes (SHARK-NIR, MAVIS), 40-m-class telescopes (MORFEO), and space missions (JUICE, PLATO). His areas of expertise include high-resolution imaging systems, coronagraphy, and adaptive optics.

Jesse Cranney is a postdoctoral adaptive optics scientist at the Advanced Instrumentation and Technology Centre, Research School of Astronomy and Astrophysics, at the Australian National University. He specializes in predictive control and estimation of multi-conjugate adaptive optics systems and calibration techniques for wide-field diffraction-limited instruments.

Valentina Viotto worked in the LINC-NIRVANA instrument AIV and commissioning and then focused on feasibility studies of novel AO concepts, such as GMCAO and INGOT WFS. She currently serves as a system engineer for the telescope units of the CHEOPS and PLATO space missions, devoted to extra-solar planet search/characterization. In the AO field, she is in charge of the MAVIS instrument’s AO module and of the development of a flexible test bench for MCAO feasibility studies.

Israel Vaughn is an instrument scientist in the Research School of Astronomy and Astrophysics. They have a background in optical instrumentation, optics for space, and polarimetric remote sensing. They have contributed to a number of ground and space optical systems, including the optical payloads for the UNSW M2 mission, the Veloce planet finding spectrograph, the MAVIS calibration unit, and the laser tomographic adaptive optics systems for the Giant Magellan Telescope. They also helped to establish the theoretical framework to treat polarimetric imaging systems as channeled communications systems. They are passionate about optics and novel optical techniques for space and astronomy.

Dionne Haynes: Biography is not available.

David Brodrick is the lead systems engineer of the MAVIS project. His background is in systems engineering and control systems engineering.

François Rigaut is the AO principal scientist at Astralis-AITC, Australian National University. He has 30 years of experience and involvement in AO systems for astronomy, from COME-ON to GeMS. He has also been active in the theory of AO, from Ground Layer Adaptive Optics to Fourier-based approach to estimating AO performance, and has authored over 350 papers in the field. He is currently the principal investigator of MAVIS for the ESO VLT.